Effective medium theory based analytical models for the potential and field distributions in arrays of nanoscale junctions

Vijaya Kumar Gurugubelli and Shreepad Karmalkar

Citation: Journal of Applied Physics **122**, 024502 (2017); doi: 10.1063/1.4991485
View online: http://dx.doi.org/10.1063/1.4991485
View Table of Contents: http://aip.scitation.org/toc/jap/122/2
Published by the American Institute of Physics

Effective medium theory based analytical models for the potential and field distributions in arrays of nanoscale junctions

Vijaya Kumar Gurugubelli[a] and Shreepad Karmalkar[b]
Department of Electrical Engineering, Indian Institute of Technology Madras, Chennai 600036, India

(Received 22 April 2017; accepted 20 June 2017; published online 11 July 2017)

Recently, we developed an Effective Medium Theory (EMT) for the Space-Charge Region electrostatics of Schottky and *p-n* junctions in arrays of nanofilms (NFs), nanowires, and nanotubes in a dielectric ambient and gave formulas for their junction depletion width and screening length characterizing the space-charge tail. In the present work, we develop this EMT further and derive simple formulas for the potential and field distributions in the semiconductor and dielectric media of the array. The formulas derived are validated with numerical simulations. It is shown that the potential and field distributions perpendicular to the junction plane in the array correspond to those in a bulk junction with an effective semiconductor medium, whose permittivity and doping are their weighted averages over the cross-sectional areas of the semiconductor and dielectric; the shapes of the cross-sections are immaterial. We also analyze a single NF junction, treating it as a limiting case of an array, and obtain the following key results. For negligible film thickness, the depletion width depends linearly on applied voltage and inverse of doping; the peak electric field depends linearly on doping and inverse of ambient permittivity and varies very gradually with applied voltage. These features of a thin film junction are remarkably different from the bulk junction, wherein the depletion width and peak field have a square-root dependence on applied voltage. *Published by AIP Publishing.* [http://dx.doi.org/10.1063/1.4991485]

I. INTRODUCTION

Currently, there is an increasing interest in fabricating electronic/optoelectronic devices in semiconductor nanofilms (NFs), nanowires (NWs), and nanotubes (NTs), to harness the unique properties of materials in the nanoscale. These nanoscale devices are made either in dimensionally reduced 3D materials (e.g., Si or GaAs nanofilm/nanowires) or in single/multiple layers of 2D materials like graphene and transition metal dichalcogenides (e.g., MoS_2, which we call a nanofilm), or in 1D structures (e.g., carbon nanotubes). With their unique features resulting from the physics at nanoscale, the NFs/NWs/NTs are found to be promising candidates for transistors,[1–5] diodes,[6–11] light emitting diodes,[12,13] photodetectors,[14–18] photovoltaics,[19–23] and sensors.[24–26]

Junctions form an inevitable part of the above devices. It is known that the electrostatics of the junction space-charge region (SCR) in semiconductor NFs/NWs/NTs is different from that in the bulk semiconductor. Several works[27–34] attempted to derive analytical models for the junction depletion width (W), and field (E) and potential (φ) distributions in NFs/NWs/NTs. In spite of these works, the following gaps remained: (1) asymmetrically doped *p-n* junctions were not analyzed; (2) there was no formula for W, E, and φ as a function of NF/NW/NT thickness; it was assumed in the prior works that the NF/NW/NT thickness is much smaller than W, and so can be neglected from the electrostatics view point; for this reason, the permittivity and volume doping of the NF/NW also do not appear in their formulas; (3) there was no formula for W, E, and φ in an array of nanoscale junctions as a function of inter-film/wire/tube separation; (4) there was no formula for the screening length characterizing the partially depleted space-charge tail in arrays of nanoscale junctions; (5) the NF/NW/NT-ambient interface charge was not considered; (6) there was no unifying theory for the SCR electrostatics of NF/NW/NT junctions; this could be because of the difference in the solution methodologies adopted; for example, Refs. 27–29 analyzed a single NF junction using conformal mapping, a mathematical technique useful to obtain two-dimensional distributions, and, hence, cannot be used to obtain the three-dimensional field/potential distributions in NWs/NTs.

To address the above issues, we recently presented[35–37] a unified analytical theory for the SCR of single and arrays of nanoscale *p–n* and Schottky junctions shown in Figs. 1(a) and 1(b). Our theory includes the effect of NF/NW/NT thickness and doping, permittivities of the semiconductor and the surrounding ambient, semiconductor-ambient interface charge, if any, and inter-film/wire/tube separation in case of arrays. Using this theory, so far, we have derived simple formulas for the depletion width and screening length and have thoroughly compared this new approach of ours with the prior derivations of Refs. 27–34. The purpose of the present work is to develop this theory further by deriving the potential and field distributions.

The Effective Medium Theory (EMT) proposed by us in Ref. 37 showed that the depletion width and the screening length characterizing the partially depleted SCR tail in the array correspond to those in a bulk junction with an effective semiconductor medium, whose permittivity and doping are

[a]Electronic mail: vkgurugubelli@gmail.com
[b]Electronic mail: karmal@ee.iitm.ac.in

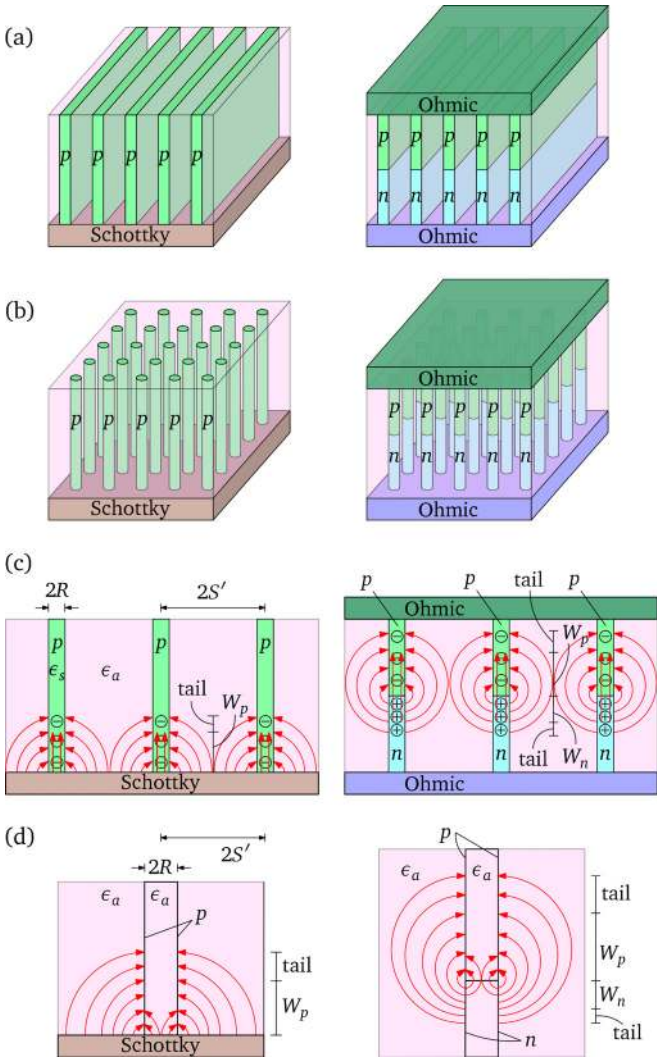

FIG. 1. Schottky and *p*-*n* junctions in an array of nanofilms (a) and nanowires (b). The cross-sections of junctions in nanofilm and nanowire arrays are identical; (c) shows these and the field lines. A nanotube array appears like (b), except that the tubes are hollow, and has the field lines shown in (d). Reproduced with permission from J. Appl. Phys. **119**, 024507 (2016). Copyright 2016 AIP Publishing LLC.

their weighted averages over the cross-sectional areas of the semiconductor and dielectric. Thus, the formulas for depletion width W_p (W_n) and screening length L_{Ap} (L_{An}) on the *p*-side (*n*-side) SCR are[37]

$$W_p = \sqrt{\frac{2\epsilon_{emt}V_p}{qN_{Aemt}}} \quad \text{and} \quad L_{Ap} = \sqrt{\frac{\epsilon_{emt}V_t}{qN_{Aemt}}},$$
$$W_n = \sqrt{\frac{2\epsilon_{emt}V_n}{qN_{Demt}}} \quad \text{and} \quad L_{An} = \sqrt{\frac{\epsilon_{emt}V_t}{qN_{Demt}}}, \tag{1}$$

where V_p (V_n) is the *p*-side (*n*-side) potential drop

$$V_p = (V_{bi} - V_a)\left(\frac{N_D}{N_A + N_D}\right), \quad V_n = V_{bi} - V_a - V_p, \tag{2}$$

V_{bi} is the built-in potential, V_a is the applied voltage, N_A (N_D) is the *p*-side (*n*-side) doping, V_t is the thermal voltage, and q is the electronic charge,

$$\epsilon_{emt} = \frac{\epsilon_s A_s + \epsilon_a A_a}{A_s + A_a}, \tag{3}$$

$$N_{Aemt} = \frac{N_A A_s + 0 \times A_a}{A_s + A_a}, \quad N_{Demt} = \frac{N_D A_s + 0 \times A_a}{A_s + A_a}, \tag{4}$$

and ϵ_s (ϵ_a) and A_s (A_a) are the permittivity and cross-sectional area of the semiconductor NF/NW/NT (ambient dielectric), respectively. Note that the formulas in Eq. (1) are similar to those in a bulk semiconductor junction having ϵ_{emt} and N_{Aemt} (N_{Demt}) as the permittivity and doping, respectively. These formulas apply independent of the shapes of the semiconductor cross-section and the lattice type describing the array.

Refer to the field pictures of Figs. 1(c) and 1(d). The present work develops the above EMT further and shows that the potential (φ) and field (E_z) distributions perpendicular to the junction plane in the nanoscale junction array also correspond to those in a bulk junction with the effective semiconductor medium, i.e.,

$$\varphi(z) = \begin{cases} \dfrac{qN_{Aemt}W_p^2}{2\epsilon_{emt}}\left(\dfrac{z}{W_p} - 1\right)^2 & p\text{-side}, \\ V_{bi} - V_a - \dfrac{qN_{Demt}W_n^2}{2\epsilon_{emt}}\left(\dfrac{z}{W_n} + 1\right)^2 & n\text{-side}, \end{cases} \tag{5}$$

$$E_z(z) = \begin{cases} \dfrac{qN_{Aemt}W_p}{\epsilon_{emt}}\left(1 - \dfrac{z}{W_p}\right) & p\text{-side}, \\ \dfrac{qN_{Demt}W_n}{\epsilon_{emt}}\left(1 + \dfrac{z}{W_n}\right) & n\text{-side}, \end{cases} \tag{6}$$

where it is assumed that *p*-side (*n*-side) lies in $z > 0$ ($z < 0$). Note that the above variations of φ and E_z with z are quadratic and linear, respectively, as in a bulk junction. Further, the EMT gives a formula for the normal electric field inside and outside the semiconductor region of the array.

Section II reviews the crucial approximations and formulas derived in our prior work[37] that form the basis for the present work. In Secs. III and IV, we derive our EMT based analytical models for NFs and NWs/NTs, respectively. In Sec. V, the models are summarized in a tabular form for the convenience of the users and are validated by comparing them with TCAD simulations.

II. REVIEW

Because of the periodic nature of the arrays, it is sufficient to analyze the unit cell of the array shown in Fig. 2 along with the coordinate axes. Figure 2 also marks the geometrical parameters that govern the electrostatics, namely - the film/wire/tube thickness $2R$ and the effective inter-film/wire/tube separation $2S$ (see Ref. 37 for more description). In deriving the depletion width and screening length models in Ref. 37, we approximated that, over the NF/NW/NT thickness, the axial field E_z and the potential φ are uniform and the normal field E_x or E_r varies linearly.[35,37] Further, we assumed the junction plane $z = 0$ to be equipotential, i.e., $\varphi(x, z = 0) = V_p$ (see Fig. 2); note that V_p denotes the potential at $z = 0$ as well as the potential drop across the *p*-region.

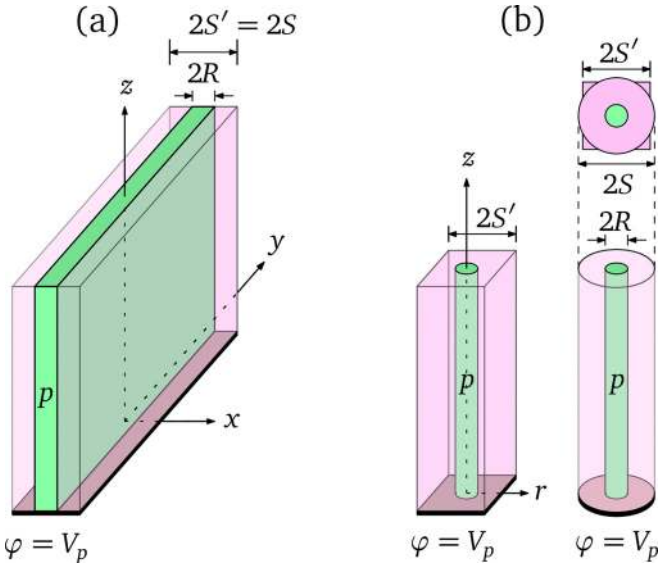

FIG. 2. (a) The simplified nanostructure of the NF array of Fig. 1(a). (b) The simplified nanostructure of the NW array of Fig. 1(b).

This equipotential condition and therefore Eq. (2) for V_p are accurate in Schottky and symmetrically doped p–n junctions ($N_A = N_D$), but are approximate in asymmetrically doped p–n junctions ($N_A \neq N_D$), and become progressively inaccurate for higher doping asymmetry and larger film/wire/tube thickness and separation. It was shown in Ref. 37 that Eq. (2) yields a fairly accurate model for the depletion width in the array of NW junctions having $N_D/N_A = 100$ and $A_a/A_s = 14$, suggesting that the EMT applies very well to practical NF/NW/NT arrays that mostly employ small film/wire/tube thickness and separation.

We employ the above assumptions in the present work too and derive equations for zero interface charge (σ_f) between the NFs/NWs/NTs and the ambient, for simplicity. However, as proved in our previous works,[35,37] the equations derived can be readily used for non-zero σ_f by replacing the doping levels in model expressions by effective doping levels, which, in case of NT arrays, are obtained by directly adding σ_f to the NT surface doping and, in case of NF/NW arrays, are obtained by distributing σ_f uniformly over the NF/NW thickness and adding it to the NF/NW volume doping.

Below we reproduce the model equations for p-side. Similar equations would apply to the n-side.

A. Array of nanofilm junctions

The potential distribution φ in the ambient surrounding the NF is[37]

$$\varphi(x \geq R, z) = V_p - \sum_{m=0}^{\infty} B_m \sin(k_m z) \frac{\cosh[k_m(S-x)]}{\cosh[k_m(S-R)]}, \quad (7)$$

where $k_m = (2m+1)\pi/2W_p$,

$$B_m = \frac{2qN_A}{\epsilon_s W_p k_m^3 \left[1 + \frac{\epsilon_a}{\epsilon_s} \frac{\tanh[k_m(S-R)]}{k_m R}\right]}, \quad (8)$$

$$\frac{W_p}{W_{pB}} = \sqrt{\alpha} \left[\sum_{m=0}^{\infty} \frac{(-1)^m/(2m+1)^3}{1 + \frac{\epsilon_a}{\epsilon_s} \frac{\tanh[k_m(S-R)]}{k_m R}}\right]^{-\frac{1}{2}}, \quad (9)$$

$$W_{pB} = \sqrt{\frac{2\epsilon_s V_p}{qN_A}}. \quad (10)$$

$$\alpha = \sum_{0}^{\infty} (-1)^m/(2m+1)^3 = \pi^3/32 \approx 0.97. \quad (11)$$

Here, W_{pB} denotes the p-side depletion width in a bulk junction.

For small R and S satisfying the following relation

$$\frac{W_p}{R} \geq \frac{\pi}{\sqrt{2}} \left(\frac{S}{R} - 1\right), \quad (12)$$

Equation (9) is approximated to the following closed-form expression[37]

$$W_p \approx \zeta W_{pB} \quad \text{where} \quad \zeta = \sqrt{1 + \frac{\epsilon_a}{\epsilon_s}\left[\frac{S}{R} - 1\right]}, \quad (13)$$

which is recast as Eq. (1) of EMT.

B. Array of nanowire and nanotube junctions

As mentioned in Ref. 37, from an electrostatic view point, an NT array is analogous to an NW array with zero space-charge but non-zero interface charge, and ϵ_s replaced by the permittivity of the medium inside the NTs. Hence, we derive the equations for NWs, which can be extended to NT arrays as detailed in Ref. 37. The potential distribution φ in the ambient surrounding the NW is[37]

$$\varphi(r \geq R, z) = V_p - \sum_{m=0}^{\infty} B_m \sin(k_m z) \times \left\{\frac{I_1(k_m S)K_0(k_m r) + I_0(k_m r)K_1(k_m S)}{I_1(k_m S)K_0(k_m R) + I_0(k_m R)K_1(k_m S)}\right\}, \quad (14)$$

where $k_m = (2m+1)\pi/2W_p$, I_0, I_1, K_0, and K_1 are modified Bessel functions, and

$$B_m = \frac{2qN_A}{\epsilon_s W_p k_m^3 \left[1 + 2\frac{\epsilon_a}{\epsilon_s} \frac{T(k_m)}{k_m R}\right]}, \quad (15)$$

$$T(k_m) = \frac{I_1(k_m S)K_1(k_m R) - I_1(k_m R)K_1(k_m S)}{I_1(k_m S)K_0(k_m R) + I_0(k_m R)K_1(k_m S)}, \quad (16)$$

$$\frac{W_p}{W_{pB}} = \sqrt{\alpha} \left[\sum_{m=0}^{\infty} \frac{(-1)^m/(2m+1)^3}{1 + 2\frac{\epsilon_a}{\epsilon_s} \frac{T(k_m)}{k_m R}}\right]^{-\frac{1}{2}}. \quad (17)$$

For small R and S satisfying the following relation

$$\frac{W_p}{R} \geq 2.7 \left(\frac{S}{R} - 1\right)^{1.11}, \quad (18)$$

Equation (17) is approximated to the following closed-form expression[37]

$$W_p \approx \zeta W_{pB} \quad \text{where} \quad \zeta = \sqrt{1 + \frac{\epsilon_a}{\epsilon_s}\left[\left(\frac{S}{R}\right)^2 - 1\right]}, \tag{19}$$

which is recast as Eq. (1) of EMT.

III. MODEL FOR ARRAYS OF NANOFILM JUNCTIONS

We analyze the p-side and extend these results to the n-side. It is sufficient to present the solution for $0 \le x \le S$ because the normal electric field $E_x = 0$ at $x = 0$ due to symmetry, so that the potential and field distributions are even and odd functions of x, respectively.

A. Distributions on the *p*-side

Using the approximation that φ is constant over the film thickness, we obtain the potential distribution inside the film by substituting $x = R$ in Eq. (7)

$$\varphi(x \le R, z) \approx V_p - \sum_{m=0}^{\infty} B_m \sin(k_m z). \tag{20}$$

The axial electric field E_z inside the ambient and the film are obtained by differentiating Eqs. (7) and (20) with respect to z

$$E_z(x \ge R, z) = \sum_{m=0}^{\infty} B_m k_m \cos(k_m z) \frac{\cosh[k_m(S-x)]}{\cosh[k_m(S-R)]}, \tag{21}$$

$$E_z(x \le R, z) = \sum_{m=0}^{\infty} B_m k_m \cos(k_m z). \tag{22}$$

The normal electric field E_x inside the ambient is obtained by differentiating Eq. (7) with respect to x

$$E_x(x > R, z) = -\sum_{m=0}^{\infty} B_m \sin(k_m z) k_m \frac{\sinh[k_m(S-x)]}{\cosh[k_m(S-R)]}. \tag{23}$$

To obtain E_x inside the film, we cannot use Eq. (20) since its derivative with respect to x is zero. Note that we obtained Eq. (20) for φ inside the film from Eq. (7) for φ outside the film by employing the constant φ approximation over the film thickness. We obtain E_x in a similar manner as follows. From the approximation that, inside the film, E_x varies linearly with x from $E_x = 0$ at $x = 0$, we have

$$E_x(x < R, z) = E_x(x = R^-, z)\left(\frac{x}{R}\right) = \frac{\epsilon_a}{\epsilon_s} E_x\left(x = R^+, z\right)\left(\frac{x}{R}\right). \tag{24}$$

Using Eq. (23) in Eq. (24), we obtain E_x inside the film

$$E_x(x < R, z) = -\left[\frac{\epsilon_a}{\epsilon_s}\sum_{m=0}^{\infty} B_m \sin(k_m z) k_m \tanh[k_m(S-R)]\right]\frac{x}{R}. \tag{25}$$

We emphasize that the above linear variation of E_x with x is not a result of the derivative of the constant φ approximation, but rather, an approximation of the derivative of the actual φ. We now derive the closed-form approximations of the above series solutions of φ, E_z, and E_x. For small R and S satisfying Eq. (12), we have $\cosh[k_m(S-x)] \approx 1$ for $x \ge R$ in Eqs. (7), (21), and (23), $\tanh[k_m(S-R)] \approx k_m(S-R)$ in Eqs. (8), (9), and (25), and $\sinh[k_m(S-x)] \approx k_m(S-x)$ in Eq. (23), resulting in

$$B_m = \frac{2qN_A}{\epsilon_s W_p k_m^3 \zeta^2}, \tag{26}$$

$$\varphi(x \ge R, z) \approx V_p - \sum_{m=0}^{\infty} B_m \sin(k_m z), \tag{27}$$

$$E_z(x \ge R, z) \approx \sum_{m=0}^{\infty} B_m k_m \cos(k_m z), \tag{28}$$

$$E_x(x > R, z) \approx -\sum_{m=0}^{\infty} B_m \sin(k_m z) k_m^2 (S-x), \tag{29}$$

$$E_x(x < R, z) \approx -\left[\frac{\epsilon_a}{\epsilon_s}\sum_{m=0}^{\infty} B_m \sin(k_m z) k_m^2 (S-R)\right]\frac{x}{R}. \tag{30}$$

Note that Eqs. (27) and (28) for inside the ambient have turned out to be the same as Eqs. (20) and (22) for inside the film.

Substituting Eq. (26) in Eqs. (20), (22), and (27)–(30) and realizing that these equations are Fourier series representations in z/W_p with a period of 4, we have

$$\sum_{m=0}^{\infty} \frac{\sin(k_m z)}{k_m^3 W_p^3} = \begin{cases} \dfrac{-1 + (z/W_p + 1)^2}{4} & \text{for } -2 \le \dfrac{z}{W_p} \le 0 \\ \dfrac{1 - (z/W_p - 1)^2}{4} & \text{for } 0 \le \dfrac{z}{W_p} \le 2, \end{cases} \tag{31}$$

$$\sum_{m=0}^{\infty} \frac{\cos(k_m z)}{k_m^2 W_p^2} = \begin{cases} \dfrac{(1 + z/W_p)}{2} & \text{for } -2 \le \dfrac{z}{W_p} \le 0 \\ \dfrac{(1 - z/W_p)}{2} & \text{for } 0 \le \dfrac{z}{W_p} \le 2, \end{cases} \tag{32}$$

$$\sum_{m=0}^{\infty} \frac{\sin(k_m z)}{k_m W_p} = \begin{cases} -\dfrac{1}{2} & \text{for } -2 < \dfrac{z}{W_p} < 0 \\ \dfrac{1}{2} & \text{for } 0 < \dfrac{z}{W_p} < 2. \end{cases} \tag{33}$$

Since the p-region lies in $z > 0$, we use the second cases from the above equations in Eqs. (20), (22), and (27)–(30) to obtain

$$\varphi(0 \le x \le S, z) \approx \frac{qN_A W_p^2}{2\epsilon_s \zeta^2}\left[\frac{z}{W_p} - 1\right]^2 = V_{pB}\left[\frac{z}{W_p} - 1\right]^2, \tag{34}$$

$$E_z(0 \le x \le S, z) \approx \frac{qN_A W_p}{\epsilon_s \zeta^2}\left[1 - \frac{z}{W_p}\right] = \frac{2V_{pB}}{W_p}\left[1 - \frac{z}{W_p}\right], \tag{35}$$

$$E_x(x > R, z) \approx -\frac{qN_A}{\epsilon_s \zeta^2}(S-x), \tag{36}$$

$$E_x(x<R,z)\approx-\frac{\epsilon_a}{\epsilon_s}\left[\frac{qN_A}{\epsilon_s\zeta^2}(S-R)\right]\frac{x}{R}=-\frac{qN_A}{\epsilon_s}\left[1-\frac{1}{\zeta^2}\right]x. \tag{37}$$

We see that the potential and the axial field, given by Eqs. (34) and (35) inside both the semiconductor and ambient, are parabolic and linear functions of z, respectively, in much the same way as in the bulk junction. We can recast Eqs. (34) and (35) in terms of N_{Aemt} and ϵ_{emt} to obtain Eqs. (5) and (6), thus arriving at an effective medium theory for the potential and field distributions in arrays of NF junctions.

From Eq. (35), the slope of E_z versus z is

$$\frac{\partial E_z}{\partial z}\approx-\frac{qN_A}{\epsilon_s\zeta^2}. \tag{38}$$

Contrast this slope with that in a bulk junction given by the Gauss's law in one-dimension, i.e., $dE/dz=-qN_A/\epsilon_s$. Thus, the slope of axial field in arrays of NF junctions is ζ^2 times smaller than the slope of electric field in a bulk junction. This is due to the fact that some of the space-charge inside the film is used up by the normal field, thus reducing the axial field and increasing the depletion width. From Eq. (35), the maximum electric field E_{zm} (m for maximum), which occurs at $z=0$ and is useful for breakdown voltage calculation, is

$$E_{zm}=\frac{qN_AW_p}{\epsilon_s\zeta^2}=\frac{qN_AW_{pB}}{\epsilon_s\zeta}=\frac{1}{\zeta}\sqrt{\frac{2qN_AV_{pB}}{\epsilon_s}}. \tag{39}$$

This maximum axial field in arrays is ζ times smaller than the maximum field $E_m=\sqrt{2qN_AV_{pB}/\epsilon_s}$ in a bulk junction. In other words, combining the models (13) for W_p, and (38) and (39) for the slope and maximum value of E_z, we can say that, for a given potential drop, the depletion width increases and the maximum value of E_z decreases by the same factor ζ from those of the bulk junction, so that the area under E_z versus z that gives the potential drop remains the same as in the bulk junction.

From Eqs. (36) and (37), we see that the normal field varies linearly with x in both semiconductor and ambient, starting from $E_x=0$ at $x=0$, reaching a maximum absolute value at $x=R^-$ or $x=R^+$ depending on ϵ_a/ϵ_s ratio, and ending at $E_x=0$ at $x=S$. It is of interest to note from Eqs. (36) and (37) that E_x is constant with z, which can be explained using the differential form of Gauss's law

$$\frac{\partial E_x}{\partial x}+\frac{\partial E_z}{\partial z}=\frac{\rho}{\epsilon}, \tag{40}$$

where ρ is the space-charge density and ϵ is the permittivity; $\rho=0$ and $\epsilon=\epsilon_a$ in the ambient, and $\rho=-qN_A$ and $\epsilon=\epsilon_s$ in the semiconductor. Since E_z varies linearly with z [see Eq. (38)] and ρ is constant over z ($=0$ or $=-qN_A$), we find from Eq. (40) that E_x depends only on x and not on z. In fact, Eqs. (36) and (37) for E_x can be derived from the Gauss's law as follows. Substitution of Eq. (38) into Eq. (40) results in

$$\frac{\partial E_x}{\partial x}=\begin{cases}\dfrac{qN_A}{\epsilon_s\zeta^2} & \text{inside the ambient,}\\ -\dfrac{qN_A}{\epsilon_s}\left(1-\dfrac{1}{\zeta^2}\right) & \text{inside the semiconductor.}\end{cases} \tag{41}$$

Using this equation and the boundary condition $E_x=0$ at $x=S$ and $x=0$, we obtain Eqs. (36) and (37).

A special case of an array is when the inter-film separation is large. In this case, each NF behaves like an isolated one. This case of isolated NF applies directly to single NF junctions, which are common in practice. Hence, it is important to derive their potential and field distributions. For this purpose, we let $S\to\infty$ in Eqs. (7) and (20) for potential, Eqs. (21) and (22) for E_z, and Eqs. (23) and (25) for E_x. Thus, we have

$$\varphi(x\geq R,z)=V_p-\sum_{m=0}^{\infty}B_m\sin(k_mz)e^{-k_m(x-R)}, \tag{42}$$

$$\varphi(x\leq R,z)\approx V_p-\sum_{m=0}^{\infty}B_m\sin(k_mz), \tag{43}$$

$$E_z(x\geq R,z)=\sum_{m=0}^{\infty}B_mk_m\cos(k_mz)e^{-k_m(x-R)}, \tag{44}$$

$$E_z(x\leq R,z)=\sum_{m=0}^{\infty}B_mk_m\cos(k_mz), \tag{45}$$

$$E_x(x\geq R,z)=-\sum_{m=0}^{\infty}B_m\sin(k_mz)k_me^{-k_m(x-R)}, \tag{46}$$

$$E_x(x\leq R,z)=-\left[\frac{\epsilon_a}{\epsilon_s}\sum_{m=0}^{\infty}B_m\sin(k_mz)k_m\right]\frac{x}{R}, \tag{47}$$

where

$$B_m=\frac{2qN_A}{\epsilon_sW_pk_m^3\left[1+\dfrac{\epsilon_a}{\epsilon_s}\dfrac{1}{k_mR}\right]}. \tag{48}$$

For very thin films or single to a few layers of 2D materials, we can approximate the film thickness to be zero; see Ref. 36 that introduces Electrostatic Thickness Index (ETI) to classify films as sheet-like, bulk-like, or intermediate-sized. Thus, for thin films, i.e., for $R\to0$, we obtain B_m from Eq. (48) by neglecting the unity term in the denominator and writing $2N_AR=N_{AS}$, where N_{AS} is the charge concentration per unit surface area of the film,

$$B_m=\frac{qN_{AS}}{W_pk_m^2\epsilon_a}. \tag{49}$$

To obtain potential and field distributions in a thin film junction, we let $R\to0$ and substitute Eq. (49) in Eqs. (42)–(46); we write below the expressions for the potential and the field along the film to contrast them from those in a bulk junction

$$\varphi(x=0,z)=V_p-\frac{4qN_{AS}W_p}{\pi^2\epsilon_a}\sum_{m=0}^{\infty}\frac{\sin\left[\dfrac{(2m+1)\pi}{2}\dfrac{z}{W_p}\right]}{(2m+1)^2}, \tag{50}$$

$$E_z(x=0,z)=\frac{2qN_{AS}}{\pi\epsilon_a}\sum_{m=0}^{\infty}\frac{\cos\left[\frac{(2m+1)\pi}{2}\frac{z}{W_p}\right]}{2m+1}, \tag{51}$$

$$E_x(x=0,z)=-\frac{2qN_{AS}}{\pi\epsilon_a}\sum_{m=0}^{\infty}\frac{\sin\left[\frac{(2m+1)\pi}{2}\frac{z}{W_p}\right]}{2m+1}=-\frac{qN_{AS}}{2\epsilon_a}. \tag{52}$$

Substitution of $z=W_p$ and $\varphi(x=0,z=W_p)=0$ from the boundary conditions in Eq. (50), we obtain the relation between W_p and V_p in a thin film junction as

$$W_p=\frac{\pi^2\epsilon_a V_p}{4GqN_{AS}}\approx\frac{2.7\epsilon_a V_p}{qN_{AS}}, \tag{53}$$

where $G=\sum_0^\infty(-1)^m/(2m+1)^2\approx 0.916$ is the Catalan's constant. This linear dependence of depletion width on potential drop and inverse doping in a thin film junction is remarkably different from the square-root dependence in a bulk junction and in an array of NF junctions with a small inter-film separation as in Eq. (1).

From Eq. (51), we see the following remarkable features regarding the field distribution in a thin film junction. Note that the summation in Eq. (51) can be regarded as a Fourier series representation of a function of z/W_p. Thus, E_z is a function of N_{AS}, ϵ_a, and z/W_p and does not depend explicitly on V_p. However, an increase in V_p increases W_p, thus scaling the E_z versus z graph horizontally along the z axis (due to the z/W_p term). The expression for peak electric field, obtained by substituting $z=0$ in Eq. (51), is a diverging series. However, in practice, the film thickness is small but nonzero, and so, the peak field takes a finite value. Since the E_z distribution scales only along the z-axis with a change in V_p for zero film thickness, we can conclude that the peak field variation with V_p is very gradual for the nonzero film thickness. Moreover, we see from Eq. (51) that the field depends *linearly* on N_{AS} and $1/\epsilon_a$. Thus, increasing the ambient permittivity ϵ_a reduces the axial field strength along the film. These features of a thin film junction are remarkably different from a bulk junction or an array of NF junctions with a small inter-film separation, where the E_z versus z scales both horizontally (z axis) and vertically (E_z axis) with a change in V_p, and that the peak field has a square-root dependence on V_p and N_A [see Eq. (39)]. The gradual variation of the peak-field with an applied voltage in a thin film junction makes it more rugged for high voltage operation than a bulk junction. Also, the above observations can be used to engineer a thin film device.

Note that Eq. (53) is more accurate and predicts about 5.5% larger values than the formula $W_p=8\epsilon_a V_p/\pi qN_{AS}$, derived by us in Ref. 36 [see Eq. (15) in Ref. 36]. This difference arises because, in Ref. 36, the W_p expression was first derived for a general film thickness, for which a closed-form expression could only be obtained by approximating the series solution using its first term. Such an approximation is not required for $R\to 0$. The linear dependence of the depletion width on the applied voltage as in Eq. (53) was experimentally observed in Refs. 38 and 39, where Ref. 38 deduces the linear dependence from the capacitance-voltage measurements and Ref. 39 directly measures the depletion width from Optical Beam Induced Current (OBIC) measurements. In Ref. 36, we validated our theory using the OBIC measurements of Ref. 39. Recently, Ref. 40 derived the above linear dependence qualitatively, instead of solving the governing differential equations with appropriate boundary conditions as done by us. Also, the slow variation of potential with z as per Eq. (50) compared to the variation in a bulk junction has been experimentally observed in Ref. 41.

B. Distributions on the *n*-side

The distributions on the n-side can be obtained from those on the p-side as follows. In our device structures, if we had n-side lying in $z>0$ with the equipotential plane $z=0$ having a potential $\varphi=V_n$, where V_n is the n-side potential drop, the n-side potential distributions in the ambient and semiconductor would be the same as Eqs. (7) and (20) with V_p replaced by V_n, N_A by N_D, W_p by W_n (n-side depletion width), and k_m by $k'_m=(2m+1)\pi/2W_n$. Since the n-side actually lies in $z<0$, we flip the sign of z in Eqs. (7) and (20) and subtract them from V_d, where V_d is the potential at $z=-W_n$ and also the total potential drop ($=V_{bi}-V_a$) across the junction. Thus, we obtain the actual n-side potential distributions as

$$\begin{aligned}\varphi(x\geq R,z)&=V_d-V_n-\sum_{m=0}^{\infty}B'_m\sin\left(k'_m z\right)\frac{\cosh\left[k'_m(S-x)\right]}{\cosh\left[k'_m(S-R)\right]}\\&=V_p-\sum_{m=0}^{\infty}B'_m\sin\left(k'_m z\right)\frac{\cosh\left[k'_m(S-x)\right]}{\cosh\left[k'_m(S-R)\right]},\end{aligned} \tag{54}$$

$$\varphi(x\leq R,z)\approx V_p-\sum_{m=0}^{\infty}B'_m\sin\left(k'_m z\right), \tag{55}$$

where we have used $V_d-V_n=V_p$, and B'_m is analogous to B_m in (8). Note that Eqs. (54) and (55) are the same as Eqs. (7) and (20) with B_m replaced by B'_m and k_m by k'_m. Therefore, the E_z and E_x expressions on the n-side would be the same as Eqs. (21), (22), (23), and (25) with B_m replaced by B'_m and k_m by k'_m. Also, W_n will be given by Eq. (9) with W_p replaced by W_n, k_m by k'_m, and W_{pB} by W_{nB}, which is the n-side depletion width in a bulk junction. The formula for W_{nB} is analogous to W_{pB} in (10), i.e.,

$$W_{nB}=\sqrt{\frac{2\epsilon_s V_n}{qN_D}}. \tag{56}$$

For small R and S satisfying Eq. (12), where W_n should be used, we obtain the following closed-form expressions for depletion width, and potential and field distributions analogous to (13), (34), (35), (36), and (37)

$$W_n\approx\zeta W_{nB}\quad\text{where}\quad\zeta=\sqrt{1+\frac{\epsilon_a}{\epsilon_s}\left[\frac{S}{R}-1\right]}, \tag{57}$$

$$\varphi(0 \le x \le S, z) \approx V_d - \frac{qN_D W_n^2}{2\epsilon_s \zeta^2}\left[\frac{z}{W_n} + 1\right]^2 = V_d - V_{nB}\left[\frac{z}{W_n} + 1\right]^2, \quad (58)$$

$$E_z(0 \le x \le S, z) \approx \frac{qN_D W_n}{\epsilon_s \zeta^2}\left(1 + \frac{z}{W_n}\right) = \frac{2V_{nB}}{W_n}\left(1 + \frac{z}{W_n}\right), \quad (59)$$

$$E_x(x > R, z) \approx \frac{qN_D}{\epsilon_s \zeta^2}(S - x), \quad (60)$$

$$E_x(x < R, z) \approx \frac{\epsilon_a}{\epsilon_s}\left[\frac{qN_D}{\epsilon_s \zeta^2}(S - R)\right]\frac{x}{R} = \frac{qN_D}{\epsilon_s}\left[1 - \frac{1}{\zeta^2}\right]x. \quad (61)$$

Note that the above equations are derived from Eqs. (20), (22), and (27)–(30) by employing the functions applicable for $z<0$ in the Fourier series Equations (31)–(33), because n-side lies in $z<0$. We can recast Eqs. (57), (58), and (59) in terms of N_{Demt} and ϵ_{emt} to obtain Eqs. (1), (5), and (6), thus arriving at an effective medium theory for the potential and field distributions in arrays of NF junctions.

IV. MODEL FOR ARRAYS OF NANOWIRE AND NANOTUBE JUNCTIONS

Using the approximation that φ is constant over the wire thickness, we obtain the potential distribution inside the wire by substituting $r=R$ in Eq. (14), which turns out to be the same as Eq. (20) with B_m given by Eq. (15). Since the form of the expressions for the potential inside the film and wire is the same, the axial electric field E_z inside the wire is given by (22) with B_m given by (15). The axial field E_z inside the ambient is obtained by differentiating Eq. (14) with respect to z

$$E_z(r \ge R, z) = \sum_{m=0}^{\infty} B_m k_m \cos(k_m z) \times \frac{K_1(k_m S)I_0(k_m r) + I_1(k_m S)K_0(k_m r)}{K_1(k_m S)I_0(k_m R) + I_1(k_m S)K_0(k_m R)}. \quad (62)$$

The normal electric field E_r inside the ambient is obtained by differentiating Eq. (14) with respect to r

$$E_r(r > R, z) = -\sum_{m=0}^{\infty} B_m \sin(k_m z)k_m \times \frac{I_1(k_m S)K_1(k_m r) - K_1(k_m S)I_1(k_m r)}{I_1(k_m S)K_0(k_m R) + K_1(k_m S)I_0(k_m R)}. \quad (63)$$

From the approximation that, inside the wire, E_r varies linearly with r from $E_r=0$ at $r=0$, we obtain E_r inside the wire from Eq. (63), in a manner analogous to obtaining Eq. (25),

$$E_r(r < R, z) = -\left[\frac{\epsilon_a}{\epsilon_s}\sum_{m=0}^{\infty} B_m \sin(k_m z)k_m T(k_m)\right]\frac{r}{R}, \quad (64)$$

where $T(k_m)$ is given by Eq. (16).

We now derive the closed-form approximations of the above series solutions of φ, E_z, and E_x. For small R and S satisfying Eq. (18), we have $T(k_m) \approx k_m R[(S/R)^2 - 1]/2$ so that B_m in Eq. (15) reduces to Eq. (26), where W_p and ζ to be used are given by Eq. (19) for wires. Using this B_m in Eq. (14), approximating the ratio involving Bessel functions to be unity, and employing the Fourier series formula of Eq. (31), the potential inside both the NW and the ambient is obtained as Eq. (34). Similarly, the axial field E_z, the slope of E_z versus z, and the maximum value of E_z inside both the NW and ambient are given by Eqs. (35), (38), and (39), respectively. Note that the closed-form expressions of potential and axial field are independent of r; further, they are parabolic and linear functions of z, respectively, as in a bulk junction. Thus, we arrive at an effective medium theory for the potential and field distributions in arrays of NW junctions.

The closed-form models for E_r inside the ambient and NW can be derived from the differential form of Gauss's law,

$$\frac{\partial E_r}{\partial r} + \frac{E_r}{r} + \frac{\partial E_z}{\partial z} = \frac{\rho}{\epsilon}. \quad (65)$$

For inside the ambient, we substitute $\partial E_z/\partial z = -qN_A/\epsilon_s\zeta^2$ from Eq. (38), $\rho=0$ and $\epsilon=\epsilon_a$ into Eq. (65), so that the resulting differential equation would have the following general solution:

$$E_r(r > R, z) = \frac{qN_A}{\epsilon_s \zeta^2}\frac{r}{2} + \frac{C_a}{r}, \quad (66)$$

where C_a is a constant. Using the boundary condition $E_r|_{r=S} = 0$ in the above equation, we have $C_a = -qN_A S^2/2\epsilon_s\zeta^2$. Substituting this C_a back in Eq. (66), we obtain the normal field inside the ambient as

$$E_r(r > R, z) = -\frac{qN_A}{2\epsilon_s \zeta^2}\left[\left(\frac{S}{r}\right)^2 - 1\right]r. \quad (67)$$

For inside the NW, we substitute $\partial E_z/\partial z = -qN_A/\epsilon_s\zeta^2$ from Eq. (38), $\rho = -qN_A/\epsilon_s$ and $\epsilon = \epsilon_s$ into Eq. (65), so that the resulting differential equation would have the following general solution:

$$E_r(r < R, z) = -\frac{qN_A}{\epsilon_s}\left(1 - \frac{1}{\zeta^2}\right)\frac{r}{2} + \frac{C_s}{r}, \quad (68)$$

where C_s is a constant. Using the boundary condition $E_r|_{r=0} = 0$ in the above equation, we have $C_s=0$. Thus, the normal field inside the NW is

$$E_r(r < R, z) = -\frac{qN_A}{2\epsilon_s}\left(1 - \frac{1}{\zeta^2}\right)r. \quad (69)$$

Note that the closed-form E_r expressions are independent of z, and that $E_r(r = R^+)$ obtained from Eq. (67) and $E_r(r = R^-)$ obtained from Eq. (69) differ by the factor ϵ_a/ϵ_s, which accounts for the difference in permittivities. The E_r equation (69) inside the NW is similar to E_x equation (37) inside the NF, except that there is an extra factor of 2 in the denominator of Eq. (69), which is due to the additional E_r/r term in the Gauss's law in a cylindrical coordinate system [compare Eqs. (40) and (65)].

TABLE I. Summary of the important analytical models for *p*-side. Analogous formulas apply to *n*-side.

	Inside semiconductor			
	Series model		Closed-form model	
	NF	NW/NT	NF	NW/NT
Depletion width W_p	Eq. (9)	Eq. (17)	Eq. (13)	Eq. (19)
Screening length L_{Ap}	…	…	Eq. (1)	
Potential φ	Eq. (20)		Eq. (34)	
Axial electric field E_z	Eq. (22)		Eq. (35)	
Normal electric field E_x or E_r	Eq. (25)	Eq. (64)	Eq. (37)	Eq. (69)
	Inside surrounding ambient			
	Series model		Closed-form model	
	NF	NW/NT	NF	NW/NT
Potential φ	Eq. (7)	Eq. (14)	Eq. (34)	
Axial electric field E_z	Eq. (21)	Eq. (62)	Eq. (35)	
Normal electric field E_x or E_r	Eq. (23)	Eq. (63)	Eq. (36)	Eq. (67)

The *n*-side distributions can be obtained in the same way as done for NF array.

V. RESULTS AND VALIDATION

We summarize the important analytical models in Table I for the convenience of users. Below, we point out three important aspects of our analytical theory that make it more valuable than any numerical simulations of different device configurations: (1) It reveals new physics which is often difficult to obtain entirely from numerical simulations even if these are large in number; the effective medium theory revealed from our formulas illustrates the power of an analytical model. (2) It identifies the normalized variables (e.g., S/R and R/W_p in our work), which control the device physics, thereby enabling a compact representation of the data regarding device performance over wide operating range and device geometries and facilitating verification of the theory using relatively few experiments. (3) It can motivate new device structures, e.g., recently[42] we proposed a Schottky power rectifier which uses an array of semiconductor wires in a dielectric medium; the breakdown voltage of this device can be obtained using our theory, exemplifying the role of analytical models. Perhaps, the techniques/concepts developed in our theory for *p*–*n* and Schottky junctions can be translated to the more intriguing cases, e.g., a three terminal device like field-effect transistor (FET), or the electrostatics of a carbon nanotube FET analysed in Ref. 43.

Figure 3 shows the validity of our closed-form models considering asymmetrically doped *p*–*n* junctions realized in silicon NF and NW arrays in SiO_2 ambient and reverse biased at 20 V; values employed are $R = 50$ nm, $S/R = 3$, $N_A = 10^{16}$ cm^3, and $N_D = 5 \times 10^{16}$ cm^3. We see that our models agree well with simulations.

Figure 3(a) shows the simulated and modeled space-charge distributions inside the semiconductor. The analytical models are based on complete depletion approximation with the depletion widths on either side of the junction given by Eqs. (13) and (57); $\zeta = 1$ for the bulk junction and is given by Eq. (13) for the NF junctions and by Eq. (19) for the NW junctions. We see from Fig. 3(a) that our model captures the increase in the depletion width from bulk to NFs to NWs. A further validation is carried out by extracting the depletion width from the simulated space-charge in the *p*-region as follows:

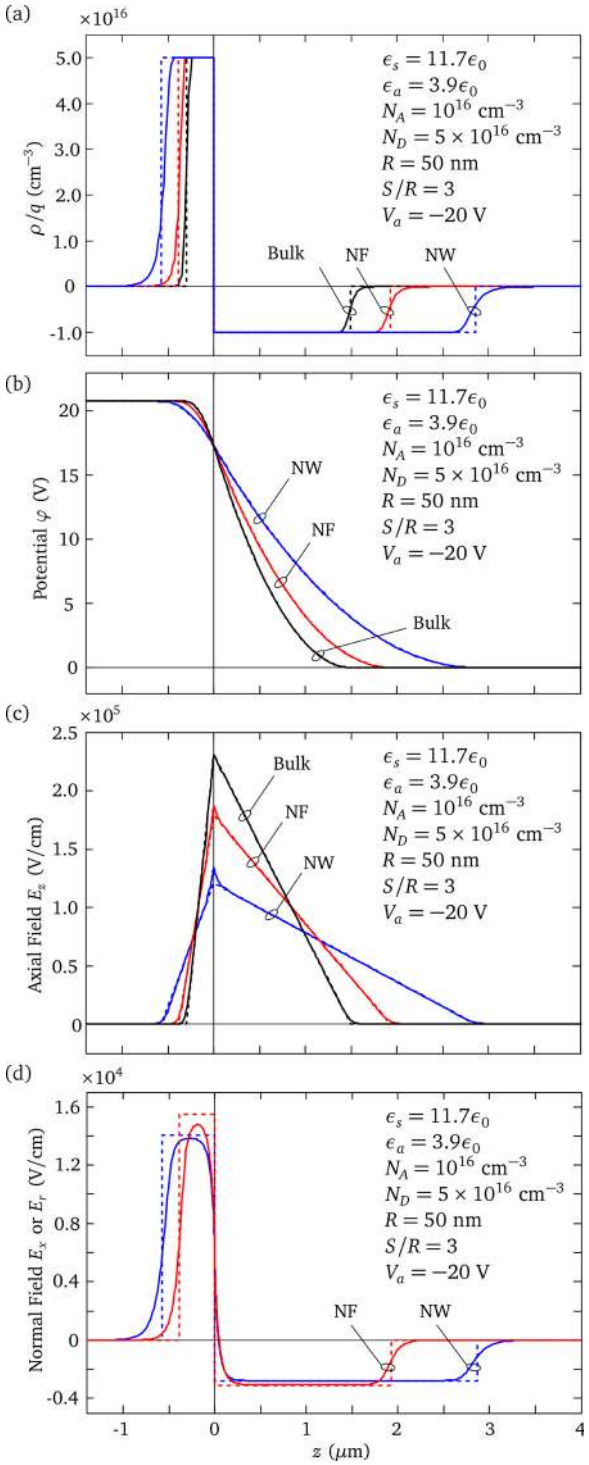

FIG. 3. Simulated distributions (solid lines) and our analytical models (dashed lines) as a function of z in *asymmetric p-n* junctions realized in bulk Si, and in arrays of Si NFs/NWs in SiO_2 ambient with $R = 50$ nm, $S/R = 3$, and 20 V reverse bias. (a) Space-charge distributions; (b) potential distributions; (c) axial field distributions; (d) normal field distributions at $x, r = R^-$; the analytical models employed are Eqs. (13), (19), (34), (35), (37), and (69), and their analogous formulas on the *n*-side.

$$W_{pext} = \frac{Q'_{pF}}{2RqN_A} \quad \text{for NFs} \tag{70}$$

$$W_{pext} = \frac{Q_{pW}}{\pi R^2 qN_A} \quad \text{for NWs}, \tag{71}$$

where Q'_{pF} is the total space-charge per unit width in the p-region of the NFs and Q_{pW} is the total space-charge in the p-region of the NWs; the suffix ext stands for the extracted value from the simulator. Analogous formulas apply to the n-regions. For the structure in Fig. 3, the above formulas, with Q'_{pF} and Q_{pW} obtained from TCAD simulator, yield $W_{pext} = 1.926\,\mu$m in NFs and $W_{pext} = 2.856\,\mu$m in NWs, while our model yields $W_p = 1.931\,\mu$m in NFs and $W_p = 2.864\,\mu$m in NWs, which are within 0.3% error.

Figure 3(b) shows the simulated potential distributions and the results of our analytical models Eq. (34) on p-side and Eq. (58) on n-side, which are parabolic functions of z; $\zeta = 1$ for the bulk junction and is given by Eq. (13) for the NF junctions and by Eq. (19) for the NW junctions. We see that our models agree well with simulations.

Figure 3(c) shows the simulated axial field distributions and the results of our analytical models Eq. (35) on p-side and Eq. (59) on n-side, which are linear functions of z; $\zeta = 1$ for the bulk junction and is given by Eq. (13) for the NF junctions and by Eq. (19) for the NW junctions. We see that the field distribution and the slope and maximum value of E_z given by Eqs. (38) and (39), respectively, agree well with simulations. The area under the three curves, which gives the potential drop, is the same because the total potential drop across the junctions is the same. Note that the simulated slope of E_z at $z = 0$ in the NF/NW junctions is close to that at any z in the bulk junction because E_x and E_r are very small near $z = 0$ so that the differential form of Gauss's law for NFs/NWs will have only $\partial E_z/\partial z$, like in the bulk junction. The non-linearity in the simulated E_z close to the depletion edge is due to the space-charge tail.

Figure 3(d) shows the simulated and analytical results of the normal field distributions at $x, r = R^-$. The analytical models employed are: Eq. (37) on p-side and Eq. (61) on n-side for the NF junction, and Eq. (69) on p-side and an analogous equation on n-side for the NW junction. Note that the plots of E_x and E_r are similar to the space-charge profiles in Fig. 3(a). We see that our model agrees well with simulations. A further validation is carried out by calculating the flux due to E_x or E_r into the film or wire on p-side as follows:

$$\text{Simulated normal flux in NF/unit width} = 2\int_0^\infty E_x dz, \tag{72}$$

$$\text{Analytical normal flux in NF/unit width} = 2E_x W_p, \tag{73}$$

$$\text{Simulated normal flux in NW} = 2\pi R \times \int_0^\infty E_r dz, \tag{74}$$

$$\text{Analytical normal flux in NW} = 2\pi R \times E_r W_p, \tag{75}$$

where the factor of 2 in NFs accounts for both sides of the film. These formulas yield 1.112 V, 1.194 V, 0.242 V-μm, and 0.253 V-μm, respectively, implying a close agreement between the model and simulations.

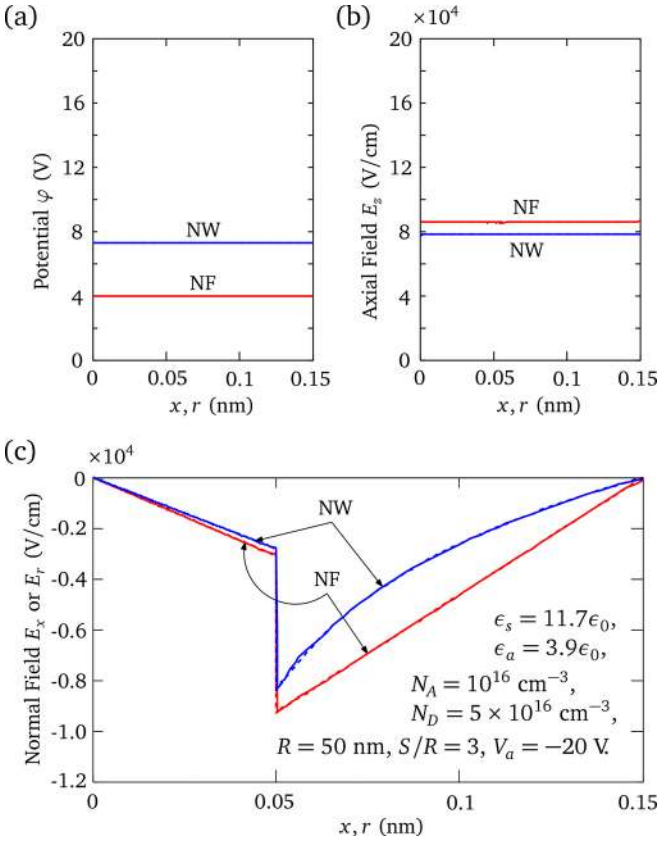

FIG. 4. Simulated distributions (solid lines) and our analytical models (dashed lines) as a function of x, r at $z = 1\,\mu$m on the p-side of the junctions in Fig. 3. (a) Potential distributions; (b) axial field distributions; (c) normal field distributions. The analytical models employed are Eqs. (13), (19), (34), (35), (36), (37), (67), and (69).

Figure 4 shows the simulated and analytical results as a function of x, r at $z = 1\,\mu$m on the p-side of the junctions in Fig. 3. We see that the analytical models agree well with simulations. Note that φ and E_z are constant for all x, r, and E_x and E_r are varying linearly with x and r inside the semiconductor. Inside the ambient, while the E_x variation is linear in NF junctions, the E_r variation is non-linear in NW junctions. Note that $E_x, E_r = 0$ at $x, r = 0, S$ because of symmetry.

Figure 5 shows the validity of our closed-form models considering an n-type Schottky junction realized in Carbon Nanotube (CNT) arrays in air ambient. In the figure, E_g denotes the energy gap of the CNT, φ_{ms} the metal-CNT workfunction difference, and N_{DS} (σ) the doping (surface-charge) per unit surface area of the nanotube. The numerical simulations are carried out in Matlab employing the methodology described in Ref. 35. The analytical models plotted in this figure are obtained by recasting the p-side equations to suit an n-type Schottky junction with $\varphi(z \to \infty) = V_{bi}$ for any applied voltage. We see that our models agree well with simulations.

VI. CONCLUSION

We derived analytical models for the potential and field distributions in the space-charge region of arrays of NF/NW/NT junctions. For small film/wire/tube thickness and inter-

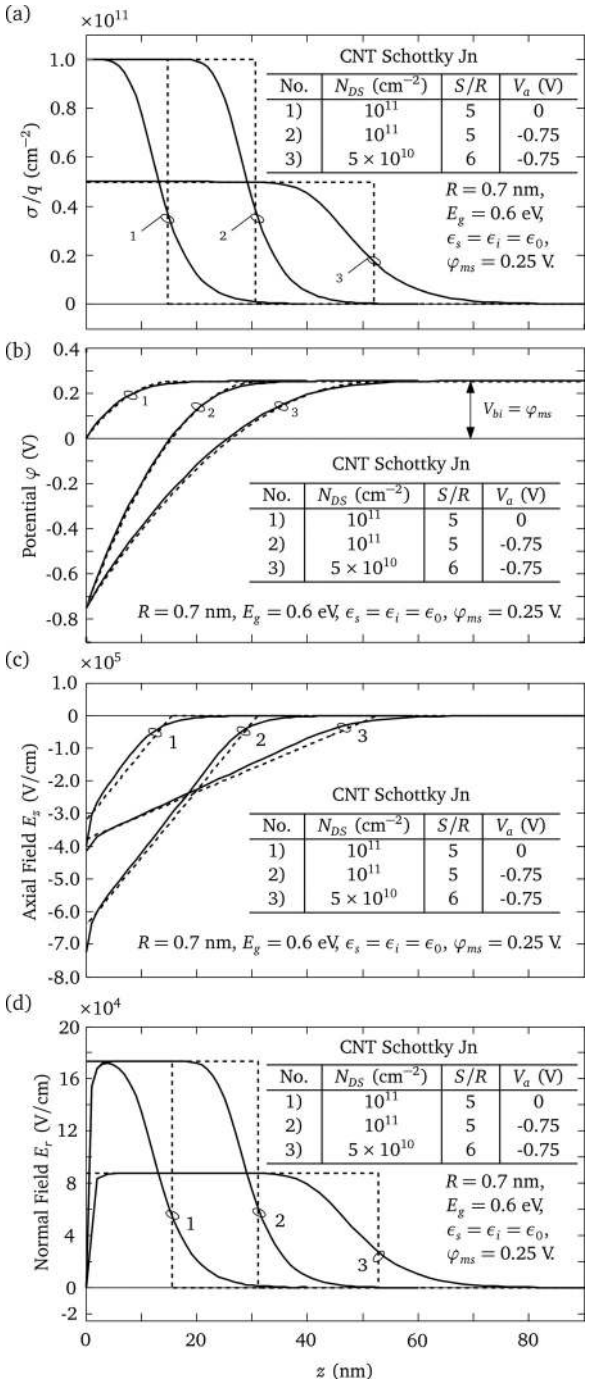

FIG. 5. Simulated distributions (solid lines) and our analytical models (dashed lines) in Schottky junctions realized in Carbon Nanotube arrays in air ambient. (a) Space-charge distributions; the box-like profiles are from the depletion width Eq. (19). (b) Potential distributions; model is Eq. (34). (c) Axial field distributions; model is Eq. (35). (d) Normal field distributions; model is Eq. (69). Note that the models are modified to suit the n-type Schottky junction with $z > 0$.

film/wire/tube separation, the analytical models are approximated to closed-form equations that conform with the Effective Medium Theory (EMT) recently proposed by us for the depletion width and the screening length in arrays of NF/NW/NT junctions. The EMT shows that the depletion width, the screening length characterizing the SCR tail, and the potential and field distributions perpendicular to the junction plane in the space-charge region (SCR) of the arrays of NF/NW/NT junctions correspond to those in a bulk junction with an effective semiconductor medium, whose permittivity and doping are their weighted averages over the cross-sectional areas of the semiconductor and dielectric; the shapes of the cross-sections are immaterial. In a single NF junction of negligible thickness, the depletion width depends linearly on applied voltage and inverse of doping; the peak electric field depends linearly on doping and inverse of ambient permittivity and varies very gradually with the applied voltage. These features of a thin film junction are remarkably different from the bulk junction, wherein the depletion width and the peak field have a square-root dependence on the applied voltage.

[1]G. Larrieu and X.-L. Han, Nanoscale **5**, 2437 (2013).
[2]J. Goldberger, A. I. Hochbaum, R. Fan, and P. Yang, Nano Lett. **6**, 973 (2006).
[3]T. Roy, M. Tosun, J. S. Kang, A. B. Sachid, S. B. Desai, M. Hettick, C. C. Hu, and A. Javey, ACS Nano **8**, 6259 (2014).
[4]S. Das, H.-Y. Chen, A. V. Penumatcha, and J. Appenzeller, Nano Lett. **13**, 100 (2012).
[5]C. Qiu, Z. Zhang, M. Xiao, Y. Yang, D. Zhong, and L.-M. Peng, Science **355**, 271 (2017).
[6]K. Q. Peng, Z. P. Huang, and J. Zhu, Adv. Mater. **16**, 73 (2004).
[7]Y. Deng, Z. Luo, N. J. Conrad, H. Liu, Y. Gong, S. Najmaei, P. M. Ajayan, J. Lou, X. Xu, and P. D. Ye, ACS Nano **8**, 8292 (2014).
[8]M. Chen, H. Nam, S. Wi, L. Ji, X. Ren, L. Bian, S. Lu, and X. Liang, Appl. Phys. Lett. **103**, 142110 (2013).
[9]M.-Y. Li, Y. Shi, C.-C. Cheng, L.-S. Lu, Y.-C. Lin, H.-L. Tang, M.-L. Tsai, C.-W. Chu, K.-H. Wei, J.-H. He *et al.*, Science **349**, 524 (2015).
[10]B. Kaestner, D. G. Hasko, and D. A. Williams, Jpn. J. Appl. Phys., Part 1 **41**, 2513 (2002).
[11]M. Hughes, K. Homewood, R. Curry, Y. Ohno, and T. Mizutani, Appl. Phys. Lett. **103**, 133508 (2013).
[12]X.-M. Zhang, M.-Y. Lu, Y. Zhang, L.-J. Chen, and Z. L. Wang, Adv. Mater. **21**, 2767 (2009).
[13]E. Lai, W. Kim, and P. Yang, Nano Res. **1**, 123 (2008).
[14]Y. Wu, X. Yan, X. Zhang, and X. Ren, Appl. Phys. Lett. **109**, 183101 (2016).
[15]A. C. Farrell, P. Senanayake, X. Meng, N. Y. Hsieh, and D. L. Huffaker, Nano Lett. **17**, 2420 (2017).
[16]S. H. Yu, Y. Lee, S. K. Jang, J. Kang, J. Jeon, C. Lee, J. Y. Lee, H. Kim, E. Hwang, S. Lee *et al.*, ACS Nano **8**, 8285 (2014).
[17]D. Kufer and G. Konstantatos, Nano Lett. **15**, 7307 (2015).
[18]Y. Liu, N. Wei, Q. Zeng, J. Han, H. Huang, D. Zhong, F. Wang, L. Ding, J. Xia, H. Xu *et al.*, Adv. Opt. Mater. **4**, 238 (2016).
[19]Z. Fan, H. Razavi, J-w. Do, A. Moriwaki, O. Ergen, Y.-L. Chueh, P. W. Leu, J. C. Ho, T. Takahashi, L. A. Reichertz *et al.*, Nat. Mater. **8**, 648 (2009).
[20]M. D. Kelzenberg, S. W. Boettcher, J. A. Petykiewicz, D. B. Turner-Evans, M. C. Putnam, E. L. Warren, J. M. Spurgeon, R. M. Briggs, N. S. Lewis, and H. A. Atwater, Nat. Mater. **9**, 368 (2010).
[21]P. Krogstrup, H. I. Jørgensen, M. Heiss, O. Demichel, J. V. Holm, M. Aagesen, J. Nygard, and A. F i. Morral, Nat. Photonics **7**, 306 (2013).
[22]J. Wallentin, N. Anttu, D. Asoli, M. Huffman, I. Åberg, M. H. Magnusson, G. Siefer, P. Fuss-Kailuweit, F. Dimroth, B. Witzigmann *et al.*, Science **339**, 1057 (2013).
[23]M.-L. Tsai, S.-H. Su, J.-K. Chang, D.-S. Tsai, C.-H. Chen, C.-I. Wu, L.-J. Li, L.-J. Chen, and J.-H. He, ACS Nano **8**, 8317 (2014).
[24]B.-R. Huang, C.-L. Hsu, Y.-K. Wang, and W.-L. Yang, IEEE Sens. J. **17**(13), 3967–3974 (2017).
[25]S.-Y. Cho, H.-W. Yoo, J. Y. Kim, W.-B. Jung, M. L. Jin, J.-S. Kim, H.-J. Jeon, and H.-T. Jung, Nano Lett. **16**, 4508 (2016).
[26]B. Liu, L. Chen, G. Liu, A. N. Abbas, M. Fathi, and C. Zhou, ACS Nano **8**, 5304 (2014).
[27]S. Petrosyan and A. Y. Shik, Sov. Phys. J. Exp. Theor. Phys. **69**, 1261 (1989).
[28]B. Gelmont, M. Shur, and C. Moglestere, IEEE Trans. Electron Devices **39**, 1216 (1992).

[29]A. S. Achoyan, A. Yesayan, E. Kazaryan, and S. Petrosyan, Semiconductors **36**, 903 (2002).
[30]A. Achoyan, S. Petrosyan, W. Craig, H. Ruda, and A. Shik, J. Appl. Phys. **101**, 104308 (2007).
[31]F. Léonard and J. Tersoff, Phys. Rev. Lett. **83**, 5174 (1999).
[32]H. Ruda and A. Shik, Appl. Phys. Lett. **85**, 1030 (2004).
[33]F. Léonard, A. A. Talin, B. Swartzentruber, and S. Picraux, Phys. Rev. Lett. **102**, 106805 (2009).
[34]F. Léonard and A. A. Talin, Nat. Nanotechnol. **6**, 773 (2011).
[35]V. K. Gurugubelli and S. Karmalkar, Appl. Phys. Lett. **104**, 203502 (2014).
[36]V. K. Gurugubelli and S. Karmalkar, J. Appl. Phys. **118**, 034503 (2015a).
[37]V. K. Gurugubelli and S. Karmalkar, J. Appl. Phys. **119**, 024507 (2016).
[38]C. Wiemann, M. Versen, and A. Wieck, J. Vac. Sci. Technol. B **16**, 2567 (1998).
[39]D. Reuter, C. Werner, A. Wieck, and S. Petrosyan, Appl. Phys. Lett. **86**, 162110 (2005).
[40]H. Yu, A. Kutana, and B. I. Yakobson, Nano Lett. **16**, 5032 (2016).
[41]C. Zheng, Q. Zhang, B. Weber, H. Ilatikhameneh, F. Chen, H. Sahasrabudhe, R. Rahman, S. Li, Z. Chen, J. Hellerstedt *et al*., ACS Nano **11**, 2785 (2017).
[42]V. K. Gurugubelli and S. Karmalkar, in *2015 73rd Annual Device Research Conference (DRC)* (IEEE, 2015), pp. 97–98.
[43]M. A. Wahab, S. H. Jin, A. E. Islam, J. Kim, J-H. Kim, W.-H. Yeo, D. J. Lee, H. U. Chung, J. A. Rogers, and M. A. Alam, ACS Nano **7**, 1299 (2013).